

Fractional regularization to improve photoacoustic tomographic image reconstruction

Prakash, Jaya; Sanny, Dween; Kalva, Sandeep Kumar; Pramanik, Manojit; Yalavarthy, Phaneendra K.

2019

Prakash, J., Sanny, D., Kalva, S. K., Pramanik, M., & Yalavarthy, P. K. (2019). Fractional regularization to improve photoacoustic tomographic image reconstruction. *IEEE Transactions on Medical Imaging*, 38(8), 1935-1947. doi:10.1109/TMI.2018.2889314

<https://hdl.handle.net/10356/105336>

<https://doi.org/10.1109/TMI.2018.2889314>

© 2019 IEEE. Personal use of this material is permitted. Permission from IEEE must be obtained for all other uses, in any current or future media, including reprinting/republishing this material for advertising or promotional purposes, creating new collective works, for resale or redistribution to servers or lists, or reuse of any copyrighted component of this work in other works. The published version is available at:
<https://doi.org/10.1109/TMI.2018.2889314>

Downloaded on 13 Mar 2024 17:45:29 SGT

Fractional Regularization to Improve Photoacoustic Tomographic Image Reconstruction

Jaya Prakash[†], Dween Sanny[†], Sandeep Kumar Kalva, Manojit Pramanik,
and Phaneendra K. Yalavarthy*, *Senior Member, IEEE*

Abstract—Photoacoustic tomography involves reconstructing the initial pressure rise distribution from the measured acoustic boundary data. The recovery of the initial pressure rise distribution tends to be an ill-posed problem in presence of noise and when limited independent data is available, necessitating regularization. The standard regularization schemes include, Tikhonov, ℓ_1 -norm, and total-variation. These regularization schemes weigh the singular values equally irrespective of the noise level present in the data. This work introduces a fractional framework, to weigh the singular values with respect to a fractional power. This fractional framework was implemented for Tikhonov, ℓ_1 -norm, and total-variation regularization schemes. Moreover, an automated method for choosing the fractional power was also proposed. It was shown theoretically and with numerical experiments that the fractional power is inversely related to the data noise level for fractional Tikhonov scheme. The fractional framework outperforms the standard regularization schemes, Tikhonov, ℓ_1 -norm, and total-variation by 54% in numerical simulations, experimental phantoms and *in vivo* rat data in terms of observed contrast/signal-to-noise-ratio of the reconstructed images.

Index Terms—Photoacoustic tomography, image reconstruction, regularization theory, fractional methods, compressive sensing.

I. INTRODUCTION

Photoacoustic tomography (PAT) also known as optoacoustic tomography is a hybrid non-invasive imaging technique which can provide optical absorption contrast at high ultrasonic resolution [1]–[5]. In PAT, a nanosecond pulsed laser source operating in the near-infrared (NIR) window, i.e., 600 – 1000 nm irradiates the biological tissue under investigation, the delivered light gets absorbed by different tissue chromophores causing an increase in the temperature (in the order of milli Kelvin). This rise in temperature generates pressure (photoacoustic (PA)) waves due to thermo-elastic expansion in the tissue. The generated PA waves propagate through the biological tissue and are detected by ultrasonic transducers placed outside the biological tissue. The measured acoustic data at the boundary of tissue becomes input to the reconstruction method for estimating the initial pressure rise distribution. This initial pressure rise map is proportional to the product of light fluence and optical absorption coefficient. The absorption coefficient is very sensitive to the tissue patho-physiology, thus revealing the patho-physiological status of the tissue under investigation at higher contrast compared to other imaging methods. PA imaging has been used extensively in the

area of oncology and pathology [3] and also enables deep tissue imaging as light penetration in the biological tissue is higher in the NIR-window compared to other optical ranges [6]. PA imaging has another advantage of being a scalable with an ability to reveal structural and functional information for both pre-clinical and clinical applications [7]–[13]. It can also be used for noninvasive monitoring of traumatic brain injury and post-traumatic rehabilitation with high-quality reconstructed images [14]. With the help of targeted contrast agents, PA imaging has been shown to be a strong contender for molecular imaging [15]–[17].

An important aspect for translating PAT to clinical/pre-clinical applications is to develop reconstruction methods that can generate accurate PA images. The acoustic inverse problem in PAT is to accurately determine the initial pressure rise distribution from the acoustic measurements. Several reconstruction algorithms exist to solve this inverse problem. Analytical algorithms including filtered backprojection and Fourier transform based reconstructions were proposed in the literature [15], [16]. Analytical algorithms are based on the spherical Radon transform which is useful for solving three-dimensional PA reconstruction problem due to low computational footprint of analytical methods. However analytical methods have a requirement of large number of data points around the target object. Large number of data points require transducer arrays with more detector elements or long data acquisition time (if single element transducer is used). Most practical cases result in limited data and in these cases, analytical reconstruction as well as time-reversal methods often suffer from inferior spatial resolution in the reconstructed image and lack desired quantitative accuracy [18], [19]. Recent emphasis has been on model-based reconstruction techniques that are capable of providing quantitatively accurate PA images in these limited data cases [15], [16], [18]–[22], which can potentially reduce data acquisition time and cost associated with transducer arrays. It is also important to note that in limited data cases, the inverse problem becomes ill-posed and requires regularization to result in meaningful solutions [15], [16], [18]–[22].

The regularization used for solving the inverse problem in limited data cases provide a balance between the residual and quantitative accuracy. Regularization constraints the solution space making model-based reconstruction schemes more robust in noisy data cases [21], [23]–[25]. The standard regularization method in PA imaging is based on Tikhonov minimization, which uses the ℓ_2 -norm of the expected solution, thus reconstructing a smoother PA image [20], [23], [26]–[28]. The regularization parameter (which balances the data-model misfit to the expected solution) in the Tikhonov regularization scheme plays an important role in determining the required resolution characteristics in the reconstructed PA image. Several methods were proposed for determination of regularization parameter in an automated fashion, such as the Morozov discrepancy principle [31], the Generalized Cross Validation (GCV) and the L-curve method [18], [21], [25], [28]. The discrepancy principle requires an estimation of noise in the experimental data for automatically choosing the regularization parameter. Note that in real experimental setting, the measurements are influenced by electronic noise and

[†]Equal Contribution

Manuscript compiled on December 14, 2018.

M.P. acknowledges support from the Singapore Ministry of Health's National Medical Research Council (NMRC/OFIRG/0005/2016: M4062012).

D. Sanny, J. Prakash, and P. K. Yalavarthy are with the Department of Computational and Data Sciences, Indian Institute of Science, C. V. Raman Road, Bengaluru-560012. *Email id of P. K. Yalavarthy is : yalavarthy@iisc.ac.in.

S. K. Kalva, and M. Pramanik are with School of Chemical and Biomedical Engineering, Nanyang Technological University, 62 Nanyang Drive, Singapore-637459

estimation of the same is possible both in the projection space and image space [29], [30]. The GCV and L-curve methods doesn't require any prior information about noise statistics as required by discrepancy principle. Further, basis pursuit deconvolution (BPD) in the framework of least-squares QR (LSQR) has been used previously in PA imaging, as the state-of-the-art technique, to perform efficient reconstruction in these limited data cases [18].

Exponential filtering of singular values was proposed in the framework of Tikhonov filtering for carrying out the image reconstruction in PAT which provides superior PA images with better quantitative accuracy and was observed to be less biased towards the regularization parameter [19]. Singular value decomposition (SVD) enables us to study how a particular filtering scheme effects the reconstructed solution by analyzing the spectral (eigen) spread of the system matrix [25]. Even the standard method (such as Tikhonov regularization) or recently proposed exponential filtering method were formulated and studied in the framework of filtering the singular values obtained from the system matrix used in PAT. Further advanced reconstruction methods based on sparse recovery (ℓ_1 -norm and total-variation (TV)) has been proposed to improve PAT reconstruction [32]–[35]. More recently, sparse recovery methods was shown to have an advantage for performing reconstruction with very less data, thereby allowing rapid three-dimensional PA acquisitions to enable real-time pre-clinical studies [32]. In this work, regularization parameter was automatically chosen using discrepancy principle during Tikhonov inversion, while empirically chosen (to result in best possible figure of merit) in the case of ℓ_1 -norm and TV based reconstruction.

However Tikhonov, TV or ℓ_1 -norm based methods assume equal weight to all singular values (in the data fidelity term) irrespective of the amount of noise in the data. But ideally, in noisy environments the lower singular values needs to be weighed lesser. This work introduces a weighting matrix to a fractional power (which can vary with noise) to result in more accurate reconstructions compared to standard methods based on Tikhonov, sparse recovery or TV. To this end, a fractional filtering framework was utilized with the help of semi-norm in the residual error during the Tikhonov regularization, ℓ_1 and total-variation based optimization. The developed fractional filtering framework was compared with standard Tikhonov, ℓ_1 -norm and total-variation based reconstruction. Here the fractional term is applied via a weighting matrix to a fractional power. The fractional power controls the amount of damping or smoothness in the reconstructed solution. Fractional Tikhonov was proven earlier to be effective for solving linear discrete ill-posed problem using closed form expression [36], [37], however the fractional power was chosen empirically. The earlier works have restricted themselves to implementing Fractional filtering in Tikhonov framework [36], [37], in this work we have extended the same to other standard state-of-the-art methods like ℓ_1 -norm and TV regularization. Further an automated way of choosing the fractional power by maximizing a figure of merit has been proposed in this work.

Specifically, the contributions of the presented work is (a) A new methodology for automatically choosing the fractional power using a simplex method (by maximizing the signal to noise (SNR)/contrast to noise (CNR) of the reconstruction) in the fractional Tikhonov scheme for PAT. Specifically the fractional power was chosen automatically using simplex method and regularization parameter was chosen automatically using discrepancy principle in the fractional Tikhonov scheme. (b) Further, it was shown mathematically that the fractional power is inversely related to the noise in the data, i.e., the fractional power reduces as the noise in the data increases in the context of fractional Tikhonov scheme, same was established with numerical simulations. (c) Implementation of the fractional TV and fractional ℓ_1 -norm schemes within the split augmented Lagrangian

shrinkage algorithm (SALSA) framework. A systematic approach was developed to automatically estimate the fractional power using a simplex method in fractional TV and fractional ℓ_1 -norm based scheme. However, the alternating direction majorization minimization (ADMM) parameters within the SALSA framework was chosen empirically to result in best possible figure of merit as automatically optimizing for all the parameters is not computationally feasible. (d) Lastly, by using numerical simulations, experimental phantom and *in vivo* data, the proposed fractional filtering framework was shown to provide better performance in terms of standard figures of merit compared to state-of-the art reconstruction methods (i.e., Tikhonov, ℓ_1 -norm and total-variation) in PAT.

II. METHODS AND MATERIALS

A. Forward Problem

The PAT forward problem computes the acoustic field given spatially varying PA source $H(\vec{r}, t)$ (ultrasonic energy deposited in the medium per unit volume and per unit time). The physical process leading to the generation of $H(\vec{r}, t)$ can be found in Refs. [15], [38].

Assuming that the medium is acoustically homogeneous and under the condition of thermal and stress confinements, the PA pressure wave $P(\vec{r}, t)$ at a point \vec{r} and time t can be written as [15],

$$\nabla^2 P(\vec{r}, t) - \frac{1}{c^2} \frac{\partial^2 P(\vec{r}, t)}{\partial t^2} = \frac{-\beta}{C_p} \frac{\partial H(\vec{r}, t)}{\partial t}, \quad (1)$$

where c is the speed of sound in the medium, β is the thermal expansion coefficient, and C_p is the specific heat. The solution to Eq. (1) can be obtained by Green's function approach [38] and other approaches such as finite-difference, finite element, and pseudo-spectral methods.

In this work, k-space pseudo-spectral method is utilized to solve the PA wave equation. The imaging grid and measured wave field on the boundary (sensor points) can be simulated with the help of open-source k-Wave toolbox [39]. The forward problem solution (to estimate the acoustic data at sensor locations) given the initial pressure rise distribution, was obtained with the help of k-wave toolbox [39]. This limited boundary measurements were then used to obtain initial pressure rise ($P(\vec{r}, 0)$) inside the imaging domain.

B. System Matrix based Approach

The process of collecting the PA data at the sensor location can be represented as a time varying causal system [24]. The impulse response of the imaging grid is stored pixel by pixel in the system matrix as columns for geometry under consideration as described in Refs. [18], [28].

The imaging grid (containing initial pressure in a discretized form) of size $n \times n$ pixels is converted into a tall column vector of size $n^2 \times 1$ by stacking all columns one below another. The initial pressure rise at these pixels (which is unknown) can be represented as x . The system matrix A having a dimension of $m \times n^2$, i.e., each column of the system matrix is the impulse response of corresponding pixel of the image in a vectorized form [28]. The time varying columns of measured data at the sensor locations (detectors) are also stacked as long column vector of dimension $m \times 1$, this is represented by b .

While generating the system matrix for numerical simulations, it was assumed that the medium has homogeneous ultrasound properties and the speed of sound is constant (1500 m/s). The computational grid having size of 501×501 pixels (50.1 mm \times 50.1 mm) with a resolution of 0.1 mm/pixel was used while generating the system matrix and 60 detectors were placed equidistantly on a circle of 22 mm radius (to represent limited data case). Although in practice, large area detectors are used, for simplicity, the detectors were assumed

to be point detectors having a center frequency of 2.25 MHz and 70% bandwidth. The imaging region was restricted to 201×201 pixels located at the center, resulting in $n^2 = 40401$. A perfectly matched layer (PML) was used to satisfy the boundary condition. The time step for data collection was 50 ns, with a total of 512 steps ($m = 512 \times 60 = 30720$). The size of the matrix \mathbf{A} ($m \times n^2$) thus becomes 30720×40401 . The forward model for the generation of acoustic data utilized a fine grid having an imaging region as 402×402 (within the computational grid of size 1002×1002). The inverse problem utilized a grid size of 201×201 (within the computational grid of size 501×501) imaging region in order to avoid inverse crime, as typically the object is in continuous domain and during PA image reconstruction the domain gets discretized to enable computations. In this work, the signals coming from outside the imaging region were not considered as water (coupling medium) absorbs very weakly in the near infrared region and the tissue under investigation is completely contained within the imaging domain.

The forward model of PA imaging can be summarized as,

$$\mathbf{A}x = b \quad (2)$$

where \mathbf{A} is the system matrix containing impulse responses of all pixels in the imaging region as columns, x is initial value of pressure at each pixel in the imaging domain, and b is the measured acoustic data on the boundary (detector locations). The singular value decomposition (SVD) of the system matrix can be represented as,

$$\begin{aligned} \mathbf{A} &= \mathbf{U}\mathbf{S}\mathbf{V}^T \\ \mathbf{A} &= \sum_{i=1}^k u_i \sigma_i v_i \end{aligned} \quad (3)$$

where k is $\min(m, n^2)$, \mathbf{U} and \mathbf{V} are left and right orthogonal matrices ($\mathbf{U}\mathbf{U}^T = \mathbf{U}^T\mathbf{U} = \mathbf{I}_m, \mathbf{V}\mathbf{V}^T = \mathbf{V}^T\mathbf{V} = \mathbf{I}_{n^2}$) with u_i and v_i representing the columns of \mathbf{U} and \mathbf{V} , respectively. \mathbf{S} is a ($m \times n^2$) diagonal matrix with non-negative diagonal elements called as singular values arranged as,

$$\sigma_1 \geq \sigma_2 \geq \dots \geq \sigma_k$$

Note that the simplest method of obtaining x will be to use back-projection, which simply becomes $x_{bp} = \mathbf{A}^T b$ [40], [41]. The quality of the reconstructed image (x_{bp}) using this method is often limited especially when limited data is available.

C. Standard Model-Based Reconstruction Methods

1) ℓ_2 -Norm Based Tikhonov Regularization: The Tikhonov regularization method is the most common method for solving discrete ill-posed inverse problems in limited-data settings. As it uses ℓ_2 -norm based regularization of the solution, it promotes the smoothness in the desired solution. The Tikhonov minimization function can be written as,

$$\Gamma_{Tikh} = \min_x (\|\mathbf{A}x - b\|_2^2 + \lambda \|x\|_2^2) \quad (4)$$

where, λ is a regularization parameter providing the balance between residue of the linear equations (first term on the right-hand side) and expected initial pressure distribution (x). Higher regularization tends to oversmooth the image, while a smaller value of λ amplifies the noise in the image. The function Γ_{Tikh} is minimized with respect to x , resulting in [18], [20],

$$x_{Tikh} = (\mathbf{A}^T \mathbf{A} + \lambda \mathbf{I})^{-1} \mathbf{A}^T b \quad (5)$$

Using SVD of \mathbf{A} (Eq. (3)), Eq. (5) can be reduced to,

$$\begin{aligned} x_{Tikh} &= (\mathbf{V}\mathbf{S}^T\mathbf{S}\mathbf{V}^T + \lambda \mathbf{I})^{-1} \mathbf{V}\mathbf{S}^T\mathbf{U}^T b \\ &= \mathbf{V}(\mathbf{S}^T\mathbf{S} + \lambda \mathbf{I})^{-1} \mathbf{S}^T\mathbf{U}^T b \\ &= \sum_{i=1}^k \frac{\sigma_i(u_i^T b)}{\sigma_i^2 + \lambda} v_i \\ &= \sum_{i=1}^k \phi(\sigma_i)(u_i^T b) v_i \end{aligned} \quad (6)$$

where, $\phi(\sigma_i)$ are the filter factors [36], [37] that can be written as,

$$\phi(\sigma_i) = \frac{\sigma_i}{\sigma_i^2 + \lambda} \quad (7)$$

The regularization parameter λ can be found using algorithms such as GCV, L-curve, or minimal residual method (MRM) [42]. Numerical experiments found that GCV and L-curve algorithms do not converge for ill-posed problems, as also observed in Ref. [28]. In this work, the discrepancy principle [25], [31] has been utilized for computing the regularization parameter. The discrepancy principle is the most widespread $\|e\|_2$ -based parameter choice method. If the ill-posed problem is consistent in the sense that $\mathbf{A}x_{true} = b_{true}$ then the amount of noise in b can be expressed as,

$$\begin{aligned} b &= b_{true} + e \\ &= \mathbf{A}x_{true} + e \end{aligned} \quad (8)$$

The idea is to choose the regularization parameter λ such that the residual norm (also known as discrepancy) is equal to *a-priori* upper bound δ for $\|e\|_2$, i.e.,

$$\|b - \mathbf{A}x_\lambda\|_2 = \delta \quad (9)$$

where, $\|e\|_2 \leq \delta$ and x_λ is the computed regularized solution [25], [36]. Alternatively,

$$F(\lambda) = \|b - \mathbf{A}x_\lambda\|_2^2 - \delta^2 = 0 \quad (10)$$

In case of Tikhonov regularization, the Eq. (10) will be reduced using singular value decomposition as follows,

$$F_{Tikh}(\lambda) = \sum_{i=1}^k \left(\frac{\lambda(u_i^T b)}{\sigma_i^2 + \lambda} \right)^2 + \sum_{j=k+1}^m (u_j^T b)^2 - \delta^2 = 0 \quad (11)$$

Eq. (11) can then be solved by Newton's Method [31] and it is implemented using open-source regularization toolbox [43]. The generalized inverse solution can be interpreted as follows: in case of sufficient noiseless independent data ($k = m = n^2$) the solution obtained during inversion is unique and exact. When $k = m < n^2$, the least norm solution will be obtained, where the noiseless data can be fitted exactly, but the solution is non-unique. Considering $k = n^2 < m$, a least square solution which is unique will be recovered, but may not fit the generic noisy data. When $k < m < n^2$ the generalized inverse solution encapsulates the behaviour of both least norm and least squares, also known as truncated singular value solution [21].

2) ℓ_1 -Norm Based Regularization: The Tikhonov method is known to generate smooth PA image, the typical PA image can be assumed to be a sparse image as it represents vasculature. Thus utilization of non-smooth regularizers, like the ℓ_1 -norm based one will result in better accurate solution. There are many approaches for performing ℓ_1 -norm based reconstruction in PAT [18], [33], [44], [45]. The ℓ_1 -norm based minimization can be written as,

$$\Gamma_{\ell_1} = \min_x (\|\mathbf{A}x - b\|_2^2 + \lambda \|x\|_1) \quad (12)$$

where, $\|\cdot\|_1$ represents the ℓ_1 -norm. In this work, the previously developed split augmented Lagrangian shrinkage algorithm (SALSA) was utilized for solving the ℓ_1 -norm based minimization in PAT, the same is explained in [45], [46]. The reconstruction parameters in the SALSA framework were chosen heuristically to result in best possible figure of merit, i.e., contrast to noise ratio.

3) Total-Variation (TV) Based Regularization: Another state of the art approach for performing reconstructions in PAT is based on total-variation (TV), wherein a constraint is applied on the edges in the PA image. Similar to ℓ_1 -norm based ones, there are many approaches for performing TV based reconstruction in PAT [34], [47]–[49]. The TV based minimization can be written as,

$$\Gamma_{TV} = \min_x (\|\mathbf{A}x - b\|_2^2 + \lambda \|x\|_{TV}) \quad (13)$$

where, $\|\cdot\|_{TV}$ represents an isotropic total-variation function. Here, the SALSA framework was utilized for solving the isotropic TV based minimization in PAT and Chambolle-Pock iteration was used for minimizing the TV function, the same is explained in Refs. [34], [46], [50]. The reconstruction parameters for performing the TV minimization in the SALSA framework is heuristically chosen to result in best possible figure of merit, i.e., contrast to noise ratio.

D. Proposed Fractional Regularization Methods

1) Fractional Tikhonov Method: The Tikhonov regularization method with ℓ_2 -penalty over-smooths the solution, i.e., loss of sharp or fine features of the reconstructed solution. Ref. [36] proposes a scheme for measuring the residual error in Tikhonov regularization with a seminorm that uses a fractional power of the Moore-Penrose pseudoinverse of $\mathbf{A}\mathbf{A}^T$ as weighting matrix. As a result, the data fidelity term in Eq. (4) penalized by fractional Tikhonov method can be rewritten as,

$$\Gamma_{frac} = \min_x (\|\mathbf{A}x - b\|_{\mathbf{W}}^2 + \lambda \|x\|_2^2) \quad (14)$$

where, $\|x\|_{\mathbf{W}} = (x^T \mathbf{W} x)^{\frac{1}{2}}$ and \mathbf{W} is symmetric positive semidefinite matrix given as,

$$\mathbf{W} = (\mathbf{A}\mathbf{A}^T)^{\frac{(\alpha-1)}{2}} \quad (15)$$

where, α represents the fractional power with $\alpha > 0$. Eq. (14) has a unique solution for all positive values of regularization parameter λ . The semi-norm $\|\cdot\|_{\mathbf{W}}$ allows the parameter α to be chosen such that the reconstruction solution from Eq. (14) is of improved image quality. Differentiating Eq. (14) with respect to x and equating to zero results in,

$$\left((\mathbf{A}^T \mathbf{A})^{(\alpha+1)/2} + \lambda \mathbf{I} \right) x = (\mathbf{A}^T \mathbf{A})^{(\alpha-1)/2} \mathbf{A}^T b \quad (16)$$

Eq. (16) can be rewritten as,

$$(\mathbf{A}^T \mathbf{W} \mathbf{A} + \lambda \mathbf{I}) x = \mathbf{A}^T \mathbf{W} b \quad (17)$$

Using the SVD of \mathbf{A} in Eq. (17) results in,

$$(\mathbf{V} \mathbf{S} \mathbf{U}^T \mathbf{U} \mathbf{S}^{\alpha-1} \mathbf{U}^T \mathbf{U} \mathbf{S} \mathbf{V}^T + \lambda \mathbf{I}) x = \mathbf{V} \mathbf{S} \mathbf{U}^T \mathbf{U} \mathbf{S}^{\alpha-1} \mathbf{U}^T b \quad (18)$$

$$(\mathbf{V} \mathbf{S}^{\alpha+1} \mathbf{V}^T + \lambda \mathbf{I}) x = \mathbf{V} \mathbf{S}^{\alpha} \mathbf{U}^T b \quad (19)$$

The solution is given by [36],

$$\begin{aligned} x_{frac} &= \sum_{i=1}^k \frac{\sigma_i^{\alpha}}{\sigma_i^{\alpha+1} + \lambda} (u_i^T b) v_i \\ &= \sum_{i=1}^k \phi_{frac}(\sigma_i) (u_i^T b) v_i \end{aligned} \quad (20)$$

The filter function of fractional Tikhonov method for $\alpha > 0$ is given by [36],

$$\phi_{frac}(\sigma) = \frac{\sigma^{\alpha}}{\sigma^{\alpha+1} + \lambda} \quad (21)$$

The hypothesis is that applying the above scaling on singular values will result in improved reconstruction compared to Tikhonov regularization method. In this work, the fractional power (α) was chosen automatically based on maximizing the SNR/CNR of the reconstructed image (note that by SNR/CNR, we mean that SNR was maximized for experimental cases and CNR was maximized for numerical simulations for automatically choosing the fractional power) using a simplex approach. The same has been detailed in the flow-chart given in Fig. 1. Further relationship between the fractional power and smoothness of the reconstructed image is established in Appendix-I.

2) Fractional- ℓ_1 Method: Fractional- ℓ_1 based reconstruction relies on minimizing the residual error to the fractional-power of the Moore-Penrose pseudoinverse of $\mathbf{A}\mathbf{A}^T$ along with using a sparsity constraint. The objective function to be minimized in the case of fractional- ℓ_1 scheme will be,

$$\Gamma_{frac\ell_1} = \min_x (\|\mathbf{A}x - b\|_{\mathbf{W}}^2 + \lambda \|x\|_1) \quad (22)$$

The fractional- ℓ_1 objective function can now be minimized in the SALSA framework, wherein two new objective function will be minimized that are given as,

$$\Gamma_{frac\ell_1-obj1} = \min_x (\|\mathbf{A}x - b\|_{\mathbf{W}}^2 + \mu \|x - v_k - d_k\|_2) \quad (23)$$

$$\Gamma_{frac\ell_1-obj2} = \min_v (\lambda \|v\|_1 + \frac{\mu}{2} \|x_{k+1} - v - d_k\|_2) \quad (24)$$

where, λ is the regularization parameter, μ is the ADMM parameter and d_k, v_k are the iterating vectors. Specifically the difference in implementing the fractional schemes inside the SALSA frameworks comes in Eq. (23), which is minimized similar to fractional Tikhonov case explained in Sec. II-D.1. Further we have automatically chosen the fractional power (α) within each iterations of fractional- ℓ_1 framework. The other reconstruction parameters like λ and μ were empirically chosen to result in best possible figure of merit i.e. SNR/CNR. The implementation details are presented in Algorithm-1.

3) Fractional-TV Method: Fractional-TV method incorporates variational penalty function as regularization, and minimizes weighted least square norm. Total variation is used to obtain a non-smooth reconstructed solution. The objective function to be minimized in fractional-TV approach is given as,

$$\Gamma_{fracTV} = \min_x (\|\mathbf{A}x - b\|_{\mathbf{W}}^2 + \lambda \|x\|_{TV}) \quad (25)$$

Again the SALSA framework is used to solve the minimization problem. The ℓ_2 -norm regularization step (i.e., Eq. (23)) in the original SALSA framework is replaced by fractional Tikhonov-type regularization to provide solutions that are not as smooth as Tikhonov scheme. Even here the fractional power (α) is chosen automatically to result in maximum SNR/CNR values. Other reconstruction parameters are chosen heuristically to result in best possible figure of merit. The algorithmic details of fractional-TV/ ℓ_1 are given in Algorithm-1.

The first step of the algorithm consists of minimizing strictly convex quadratic function (i.e., Eq. (23)). The solution for (i.e., Eq. (23)) is given by fractional Tikhonov method as,

$$x_{k+1} = \sum_{i=1}^k \frac{\sigma_i^{\alpha}}{\sigma_i^{\alpha+1} + \mu} (u_i^T b) v_i + \sum_{i=1}^k \frac{1}{\sigma_i^{\alpha+1} + \lambda} [v_i^T (v_k + d_k)] v_i \quad (26)$$

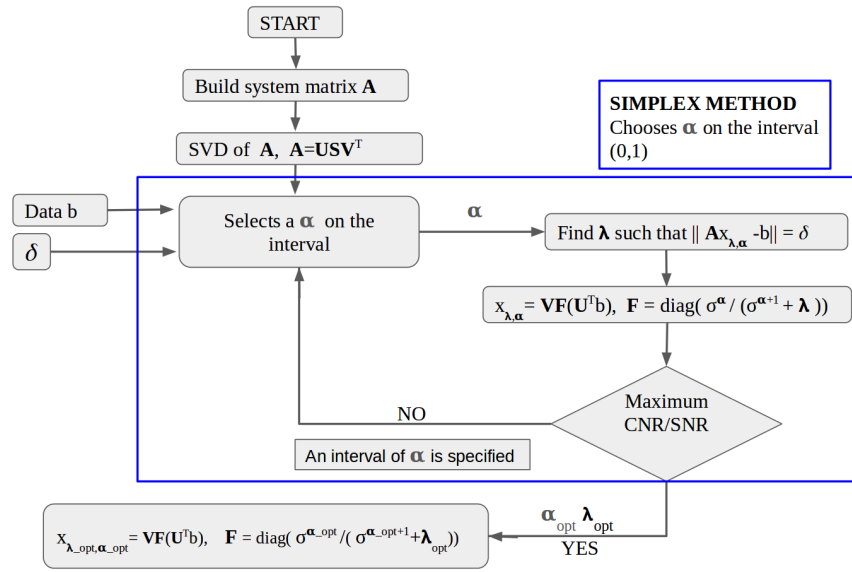


Fig. 1. Flow diagram illustrating the procedure for automatically choosing fractional power and regularization parameter in fractional Tikhonov method (Sec. II-D.1).

Algorithm 1: fractional-TV/ ℓ_1

Input: SVD of $A : U, \Sigma, V$, data b , ADMM parameter μ, d_0, v_0

Output: fractional-TV/ ℓ_1 solution x

- 1 $x_{k+1} = \min_x (\|Ax - b\|_2^2 + \mu \|x - v_k - d_k\|_2)$
Simplex method is used to determine the parameter α by maximizing SNR/CNR as explained in flow chart of Fig.1 ;
- 2 $v_{k+1} = \min_v (\lambda \psi(v) + \frac{\mu}{2} \|x_{k+1} - v - d_k\|_2)$;
($\psi(v) = \|v\|_1$ for ℓ_1 -norm minimization, and $\psi(v) = \|v\|_{TV}$ for TV minimization)
- 3 $d_{k+1} = d_k - (x_{k+1} - v_{k+1})$;
- 4 $k \leftarrow k + 1$;
- 5 until $\|Ax_{k+1} - b\|_2^2 < \delta$

The solution for the second objective function in the SALSA framework for TV based minimization is given by Moreau proximity mapping of ψ applied to $(x_{k+1} - d_k)$, and the solution is given as,

$$v_{k+1} = \Psi_{\lambda, \mu}(x_{k+1} - d_k) \quad (27)$$

Whereas minimum for the second objective function in the fractional- ℓ_1 case (Eq. (24)), $\Psi_{\lambda, \mu}$ is computed exactly which is a soft thresholding operator. But in the case of TV, $\Psi_{\lambda, \mu}$ doesn't have a closed form and $\Psi_{\lambda, \mu}$ is approximated by fixed number of Chambolle iteration [50]. The convergence of both fractional- ℓ_1 and fractional-TV is same as SALSA algorithm given in Ref. [46].

E. Figures of Merit

The efficacy of the different methods described above were quantified using the following figures of merit on numerical simulations and experimental datasets.

- 1) The Pearson correlation (PC) coefficient is a quantitative metric that measures the degree of correlation between the target and the reconstructed image [18], [19]. It is defined by:

$$PC(x_{target}, x_{recon}) = \frac{cov(x_{target}, x_{recon})}{s(x_{target})s(x_{recon})} \quad (28)$$

where, x_{target} is the expected initial pressure distribution and x_{recon} is the reconstructed initial pressure distribution. cov denotes the covariance, and s denotes the standard deviation. PC ranges between -1 to 1. Higher value of PC indicates better detectability of the targets in the reconstructed image.

- 2) Contrast-to-Noise Ratio (CNR) was also used to evaluate performance of different algorithms in numerical simulations. The contrast-to-noise ratio is a measure of the image quality based on the contrast, typically used to compare the reconstructed images [51]. The CNR is defined as [19]:

$$CNR = \frac{\mu_{roi} - \mu_{back}}{(s_{roi}^2 a_{roi} + s_{back}^2 a_{back})^{1/2}} \quad (29)$$

where, μ denotes the mean and s represents the standard deviation. The subscript roi and $back$ represent the region of interest and the background correspondingly in the reconstructed image. The area ratio is represented as $a_{roi} = \frac{A_{roi}}{A_{total}}$ and $a_{back} = \frac{A_{back}}{A_{total}}$.

- 3) In case of experimental data, the signal to noise ratio (SNR) was used to evaluate the performance of different reconstruction scheme as the expected distribution is unknown, the SNR is given as,

$$SNR = 20 \log_{10} \left(\frac{x_{signal}}{x_{noise}} \right) \quad (30)$$

where, x_{signal} are the pixels corresponding to the reconstructed region of interest in the PA image and x_{noise} are the pixels corresponding to the background noise in the reconstructed PAT image.

- 4) For quantitatively comparing the performance of different reconstruction methods in case of numerical simulations, root mean square error (RMSE) figure of merit was utilized. RMSE can be defined as,

$$RMSE = \frac{\sqrt{\sum_i^{4n^2} (x_{truth}^i - x_{recon}^i)^2}}{4n^2} \quad (31)$$

where x_{truth} indicates the ground truth and x_{recon} represent the reconstructed image.

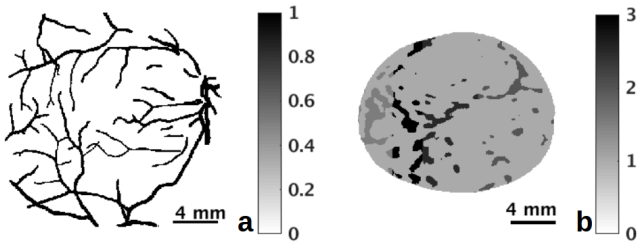


Fig. 2. Numerical phantoms used in this work. a) Blood vessel phantom, b) Realistic Breast phantom.

F. Numerical Simulations and Experimental data

1) *Numerical Simulations*: Two numerical phantoms (shown in Fig. 2) were considered for comparing the quantitative accuracy of the different reconstruction algorithms. A numerical blood vessel phantom (uni-polar in nature) with initial pressure rise of 1 kPa was used to evaluate the performance of different methods. Secondly a realistic numerical breast phantom (multi-polar in nature) created from contrast-enhanced magnetic resonance (MR) imaging data was also used for the evaluation [52].

A K-wave based forward model [39] was used for generating the acoustic data (i.e. *b*), a fine computational grid having a size of 50.1×50.1 mm (discretized to 1002×1002 pixels) was utilized and the imaging region used for numerical phantoms was 20.1×20.1 mm, this imaging region had a grid size of 402×402 pixels [39]. In order to avoid inverse crime, the collected data was reconstructed on a 201×201 grid. **For obtaining the numerically simulated data**, sixty detectors having 70% bandwidth and a center frequency of 2.25 MHz, are placed equi-distantly on a circle of radius 22 mm from the center of the imaging region. The data was sampled at 50 ns with the total time samples being 512. Gaussian noise was added to the in-silico forward data to result in SNR's of 20 dB, 40 dB, and 60 dB. A Linux workstation with dual six-core Intel Xeon processor having a speed of 2.66 GHz with 64 GB RAM was used to perform the described reconstructions.

2) *Experimental data*: The experimental setup used for PAT is shown in Fig. 2 of Ref. [40]. A Q-switched Nd:YAG laser operating at 532 nm was used to deliver laser pulses having pulse width of 5 ns with 10 Hz repetition rate. The laser pulses were delivered on the sample with the help of Four right-angle uncoated prisms (PS911, Thorlabs) and one uncoated Plano-concave lens (LC1715, Thorlabs). The light fluence on the phantom was measured to be about 9 mJ/cm^2 ($< 20 \text{ mJ/cm}^2$: ANSI safety limit [53]). A triangular shaped horse hair phantom was utilized for imaging. The side-length and diameter of hair are 10 and 0.15 mm, respectively. The hair phantom was glued to the pipette tips adhered on acrylic slab [54]. A 2.25 MHz flat ultrasound transducer (Olympus-NDT, V306-SU) of 13 mm diameter active area and $\sim 70\%$ nominal bandwidth was rotated over 360° around the sample for recording the **PA** signals. The acquired PA signals were first amplified and filtered using a pulse amplifier (Olympus-NDT, 5072PR) and then recorded using a data acquisition (DAQ) card (GaGe, compuscope 4227) having a sampling frequency of 25 MHz. Synchronization of data acquisition with laser illumination was achieved using a sync signal from laser. The reconstructed **PA** imaging region has a size of $40 \text{ mm} \times 40 \text{ mm}$ containing 200×200 pixels. **For the experimental data, a system matrix having a dimension of 51200×40000 (51200: 512 time samples for 100 detector positions and 40000: 200×200 reconstruction grid) was used.** The same setup was used to acquire the experimental *in-vivo* rat brain data.

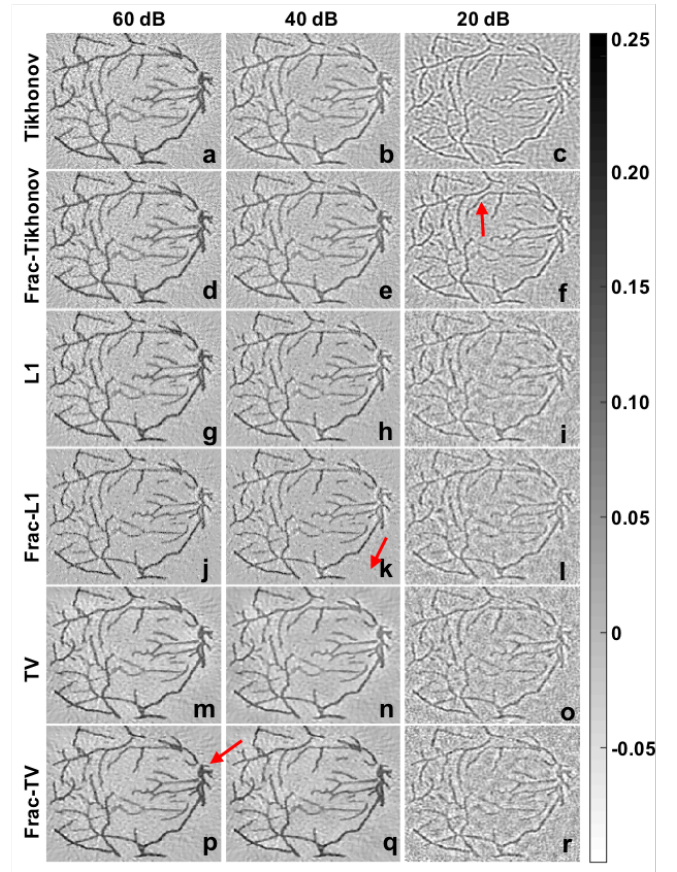


Fig. 3. Reconstruction results with simulated blood vasculature phantom (target is shown in Fig. 2(a)). a-c) shows the results using the Tikhonov reconstruction scheme with simulated data having an SNR of 60 dB, 40 dB and 20 dB, respectively. d-f) shows the results using the fractional Tikhonov reconstruction scheme with simulated data having an SNR of 60 dB, 40 dB and 20 dB, respectively. g-i) shows the results using the ℓ_1 -regularization scheme with simulated data having an SNR of 60 dB, 40 dB and 20 dB, respectively. j-l) shows the results using the fractional- ℓ_1 reconstruction scheme with simulated data having an SNR of 60 dB, 40 dB and 20 dB, respectively. m-o) shows the results using TV reconstruction scheme with simulated data having an SNR of 60 dB, 40 dB and 20 dB, respectively. p-r) shows the results using the fractional-TV scheme with simulated data having an SNR of 60 dB, 40 dB and 20 dB, respectively.

III. RESULTS

Figure 3 shows the reconstruction results with simulated blood vasculature phantom. Figs. 3(a), (b), and (c) shows the results using the Tikhonov reconstruction scheme with simulated data having an SNR of 60 dB, 40 dB, and 20 dB respectively. Figs. 3(d), (e), and (f) indicates the PAT images generated using the proposed fractional Tikhonov framework (Sec. II-D.1) with the simulated data having an SNR of 60 dB, 40 dB, and 20 dB respectively. Figs. 3(a)-(f) illustrates that the fractional Tikhonov method outperforms the standard Tikhonov reconstruction in highly noisy environment (indicated by red arrow in Fig. 3f) with an advantage of converging to similar solution in low-noise cases. Note that automatically chosen α 's in fractional Tikhonov scheme for the 60 dB, 40 dB, and 20 dB cases are 0.7611, 0.5893, and 0.1305, respectively, this indicates that the fractional power is inversely proportional to data noise level for fractional Tikhonov reconstruction. Figs. 3(g), (h), and (i) are reconstructions obtained using the ℓ_1 -norm based reconstruction scheme with simulated data having an SNR of 60 dB, 40 dB, and 20 dB respectively. Figs. 3(j), (k), and (l) are the initial pressure rise

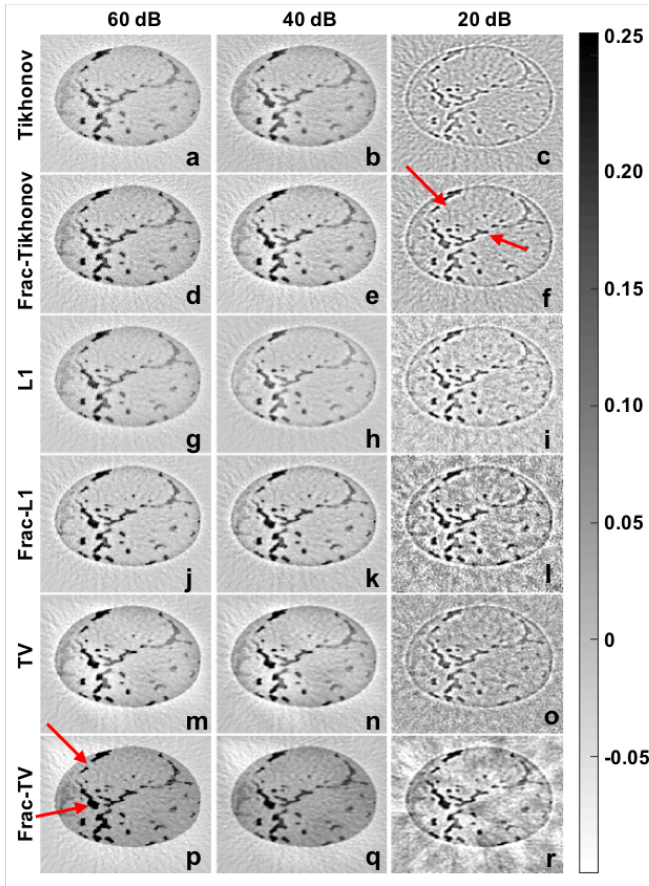


Fig. 4. Same effort as Fig. 3 with simulated Breast phantom shown in Fig. 2(b).

distributions obtained using the fractional- ℓ_1 framework (Sec. II-D.2) with the in-silico data having an SNR of 60 dB, 40 dB, and 20 dB, respectively. Figs. 3(g)-(l) illustrates that fractional framework results in better reconstruction than standard ℓ_1 -norm based method and is superior in terms of suppressing the noise, as shown by red arrow in Fig. 3(k). The reconstruction results using TV based algorithm on simulated data having an SNR of 60 dB, 40 dB, and 20 dB is given in Figs. 3(m), (n), and (o), respectively. Lastly, Figs. 3(p), (q), and (r) shows the PA images with the fractional-TV method (Sec. II-D.3) on simulated data having an SNR of 60 dB, 40 dB, and 20 dB, respectively. Overall, Fig. 3 demonstrates that fractional framework converges to more accurate solution with superior image quality when compared to standard methods (Sec. II-C). Specifically fractional-TV based methods showed greater superiority in low-noise cases and fractional Tikhonov method performed well in high noise environments.

Figure 4 shows the reconstruction results with a realist numerical breast phantom case having multi-polar characteristics. Figs. 4(a), (b), and (c) indicates the reconstruction results corresponding to Tikhonov method with simulated data having an SNR of 60 dB, 40 dB, and 20 dB, respectively. Figs. 4(d), (e), and (f) are PAT images generated using the proposed fractional Tikhonov framework with the numerical data having an SNR of 60 dB, 40 dB, and 20 dB, respectively. Figs. 4(a)-(f) shows the potential of fractional Tikhonov method over the standard Tikhonov scheme in accurately reconstructing the structures even in an highly noisy environment (indicated by red arrows in Fig. 4(f)). Figs. 4(g), (h), and (i) are reconstructions obtained using the ℓ_1 -norm based algorithm on data generated from breast phantom

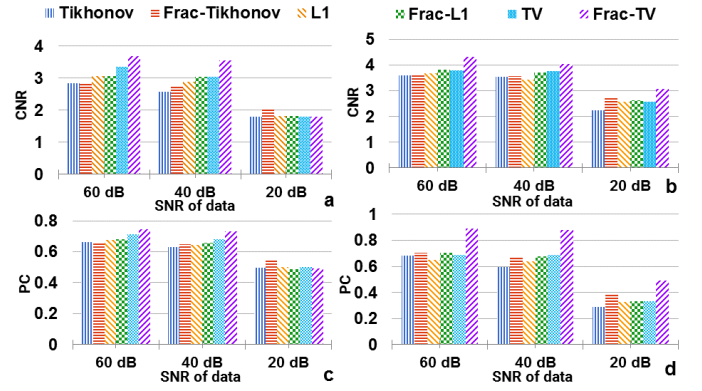


Fig. 5. Figures of merit for numerical phantom case results shown in Figs. 3 and 4. a) CNR comparison with numerical blood vessel. b) CNR comparison with numerical breast phantom case. c) PC comparison with numerical blood vessel shown in Fig. 2(a). d) PC comparison with numerical breast phantom shown in Fig. 2(b).

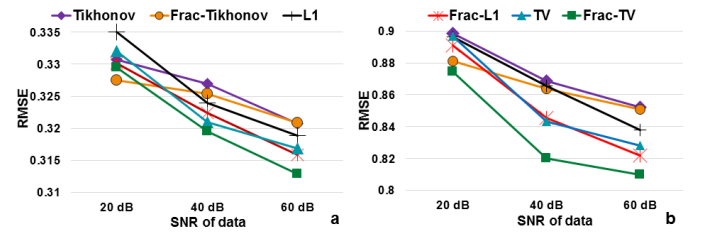


Fig. 6. Root mean square error (RMSE) comparison for a) numerical blood vessel case (reconstruction results are shown in Fig. 3) b) numerical breast phantom case (reconstruction results are shown in Fig. 4).

having a SNR of 60 dB, 40 dB, and 20 dB, respectively. Figs. 4(j), (k), and (l) are the initial pressure rise distributions corresponding to the fractional- ℓ_1 framework with the numerical data having an SNR of 60 dB, 40 dB, and 20 dB, respectively. As can be seen, the fractional- ℓ_1 framework provides higher contrast compared to standard ℓ_1 -norm based method. The reconstructions corresponding to numerical breast phantom with TV based method on simulated data having an SNR of 60 dB, 40 dB, and 20 dB, are given in Figs. 4(m), (n), and (o), respectively. Figs. 4(p), (q), and (r) shows the PA images with the fractional-TV method on simulated data having a SNR of 60 dB, 40 dB, and 20 dB respectively. Overall, Fig. 4 reveals that fractional framework converges to more accurate solution having superior image quality when compared to standard often used state-of-the-art reconstruction method. For the breast phantom case, the α 's in fractional Tikhonov scheme for the 60 dB, 40 dB, and 20 dB, cases are 0.5784, 0.2151, and 0.1759, respectively, again the fractional power reduced by increasing the data noise level.

Even in case of breast phantom case fractional-TV based methods showed greater superiority in low-noise cases and fractional Tikhonov method performed well in high noise environments as indicated by red arrows in Fig. 4. From Fig. 4, it is apparent that fractional methods are able to recover the varying contrast levels accurately compared to standard reconstruction schemes (Fig. 4(p) vs Fig. 4(m)). Moreover, the automatically chosen fractional power values were lower in the case of breast phantom in comparison with the blood vessel phantom indicating that the fractional power depends on the target image to be reconstructed. Fig. 5 indicates the CNR and PC comparison of the different reconstruction methods with the numerical blood vasculature (Fig. 3) and simulated breast phantom case (Fig. 4), the CNR values demonstrates that the proposed fractional power based framework is on-par/outperform the standard Tikhonov, TV and

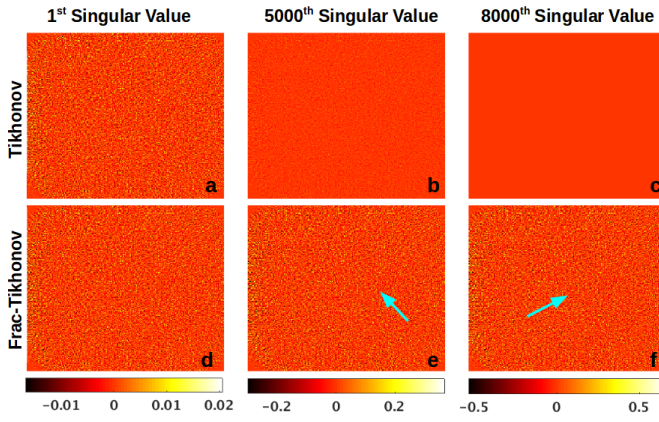


Fig. 7. Eigen modes comparison for Tikhonov and fractional Tikhonov scheme. Eigenmode pertaining to 1st singular value for a) Tikhonov and d) fractional Tikhonov method. Eigenmode corresponding to 5000th singular for b) Tikhonov and e) fractional Tikhonov method. Eigenmode for 8000th singular for c) Tikhonov and f) fractional Tikhonov method.

ℓ_1 -norm based reconstruction framework. Similarly, the PC values indicate that fractional-TV is performing better in low-noise cases while fractional-Tikhonov show superior results in high-noise case. Further, quantitative comparison of the performance of different reconstruction methods via utilization of RMSE as metric was performed. The RMSE values were plotted in Fig. 6. As expected the fractional Tikhonov method converged to Tikhonov scheme in low-noise environment. However a similar trend was not observed for ℓ_1 -norm and TV based reconstructions, as these methods are non-linear, do not have closed form solutions and relies on iterative methods. Notable in high-noise cases, the fractional framework outperformed the standard reconstruction methods.

Figure 7 indicates the eigen modes for Tikhonov and fractional Tikhonov based reconstruction. The i^{th} eigen mode is calculated as, $EM_i = \sigma_i V u_i$. As can be seen from Figs. 7(a), and (d), both fractional Tikhonov and Tikhonov method shows similar distribution while weighting the solution corresponding to larger singular values. But as we move to lower singular values in the Tikhonov framework, i.e., Figs. 7(b), and (c), the contribution from lower singular values are smoothed out, therefore in a noisy environment the high frequency content (edges) tends to get suppressed and even the contrast will be defined by only the higher singular values. In contrary with the fractional Tikhonov framework, i.e., Figs. 7(e), and (f), there is sufficient contribution from the lower singular values as indicated by cyan arrows in Fig. 7, which allows us to reconstruct high frequency information having higher contrast even in noisy environments.

Next, fractional framework utilization in experimental setting was tested. Fig. 8 indicates the reconstruction results with different methods (Sec. II-C and II-D) using the horse hair phantom. Figs. 8(a), (b), and (c) illustrate the reconstruction results corresponding to Tikhonov, ℓ_1 -norm and TV based methods using horse hair phantom. The SNR's for each of these methods are indicated below each image. Figs. 8(d), (e), and (f) shows the initial pressure rise distribution corresponding to the developed fractional Tikhonov, fractional- ℓ_1 and fractional-TV based algorithms along with the SNR's indicated below the image. Tikhonov reconstruction produces artifacts indicated by red arrow in Fig. 8(a), which seems to have reduced using the fractional Tikhonov based reconstruction (indicated by red arrow in Fig. 8(d)). Moreover the ℓ_1 -norm and TV based methods were able to generate reconstructions devoid of these artifacts, with ℓ_1 -norm reconstructions being more discontinuous (and having speckle pattern) compared to TV based reconstruction. However the fractional

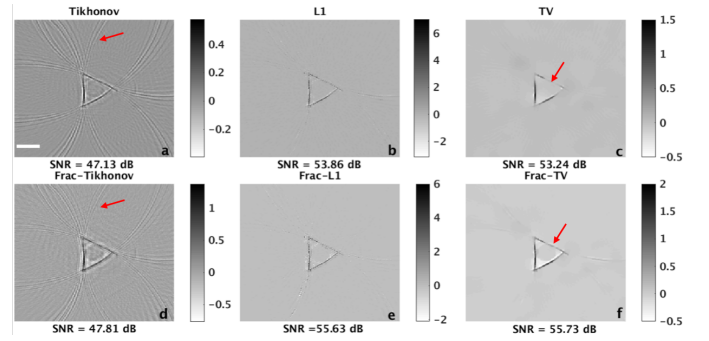


Fig. 8. Reconstructed PA images using experimental horse hair phantom data with a) Tikhonov, b) ℓ_1 -regularization, c) TV, d) fractional Tikhonov, e) fractional- ℓ_1 , and f) fractional-TV. The SNR of these reconstructed images is indicated below. Scalebar shown in Fig. 8(a) is 5 mm.

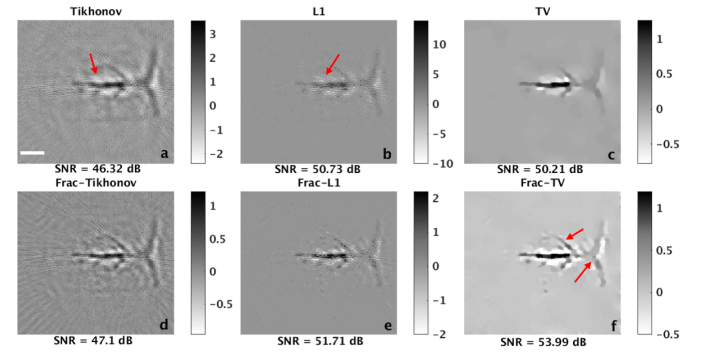


Fig. 9. Reconstructed initial pressure rise distribution using experimental *in vivo* rat brain data with a) Tikhonov, b) ℓ_1 -regularization, c) TV, d) fractional Tikhonov, e) fractional- ℓ_1 , and f) fractional-TV. The SNR of these reconstructed images is indicated below. Scalebar shown in Fig. 9(a) is 5 mm.

counterparts of ℓ_1 -norm and TV based algorithms seems to produced much better reconstruction devoid of artifacts as in Tikhonov scheme and more continuous distribution (indicated by red arrow in Fig. 8(f)). Importantly SNRs of reconstruction results using the fractional framework were much higher compared to standard reconstruction methods, improving more than 33.2%.

Lastly, the fractional regularization methods were evaluated using *in vivo* rat brain imaging to verify if the proposed framework could add value for performing real biological studies. Figure 9 illustrates the reconstruction results using different algorithms for *in vivo* brain PA imaging. The reconstruction results pertaining to Tikhonov and ℓ_1 -norm based methods are very noisy as indicated by red arrow in Figs. 9(a), and (b). However, the fractional Tikhonov and fractional- ℓ_1 based methods were able to generate reconstruction results that have lesser noise (compared to Tikhonov and ℓ_1 -norm reconstructions), the same can be seen in Figs. 9(d), and (e). On the other hand, Fig. 9(c) show the TV based reconstruction with *in vivo* brain data, which seems to be more blurry due to the piece-wise constraint applied in TV based minimization. Finally the fractional-TV based reconstruction is demonstrated in Fig. 9(f), the inferior cerebral vein, superior sagittal sinus and transverse sinus can be inferred clearly using the fractional-TV method as indicated by red arrows in Fig. 9(f). The SNR using each of the methods is given below each image. The SNR values indicate that the fractional framework seems to generate PA images with greater image quality compared to standard reconstruction methods.

IV. DISCUSSION

Quantitative **PAT** involves solving two inverse problems: one acoustical and one optical. Acoustic inversion problem involves retrieving the absorbed optical energy distribution in the tissue by measuring the tomographic acoustic waves. As the deposited energy is proportional to the optical absorption coefficient, the optical inverse problem involves turning the acoustic reconstruction into a quantified image of the optical absorption coefficient. In order to solve the acoustic inverse problem associated with **PAT** numerous inversion techniques have been developed: time-domain (back-projection) algorithms, frequency-domain algorithms, time-reversal algorithms, and model-based algorithms. Model-based algorithms represent the most general category of algorithms which has a better performance over analytical and time-reversal solutions especially in limited data cases [15], [19], [20]. The requirement of model based reconstruction techniques is a existence of a linear relation between the optoacoustic source and the measured acoustic wave fields. Thus any linear effect which is related to the pressure wave propagation or to the acoustic detection can be included in the system matrix of the model-based algorithm. This helps us to take into account the finite detection apertures or more generally, any spatio-temporal detection response in the inversion technique, as long as it can be modeled or measured. The model plays an important role in improving the reconstruction performance, which accurately accounts for the physics of the PA wave generation, propagation, and detection. Post-processing of model-based reconstructed images are performed in order to improve the reconstruction performance. This post-processing can be performed by applying deconvolution or other image enhancement schemes. Additional computational burden in performing the deconvolution step is justified as they provide much desired quantification in the reconstructed PA images.

Furthermore standard model-based reconstruction methods, i.e., Tikhonov, ℓ_1 -norm, and TV are widely used to perform reconstruction in **PAT** [18], [19], [34]. These standard methods are known to generate accurate reconstructions in low noise environment, as both larger and smaller singular values are treated similarly irrespective of data noise levels. Generalized regularization schemes, which weigh the data-fidelity or prior information also manipulate the singular values to obtain accurate solution [55], however these generalized schemes are a different class from fractional methods and the same is explained in Appendix-III. In this work, an effective way of performing PA image reconstruction with the help of fractional regularization scheme was presented, which can parameterize the singular value filtering by taking fractional powers of the spectrum during the inversion. Importantly in this work, the fractional power was chosen automatically using a simplex method based on maximizing figure of merit like SNR/CNR. It was demonstrated with numerical experiments that the fractional power varies by varying the SNR of the acquired **PA** data in fractional Tikhonov scheme. Specifically, it was observed that the fractional power reduces by increasing the noise in the data and the same was theoretically established as explained in Appendix-II. More importantly, with $\alpha = 1$, this method will yield results same as standard Tikhonov filtering, assuring that the proposed framework is more generic. However establishing similar trend with fractional- ℓ_1 /TV methods would be difficult as analytical closed form solution does not exist for these framework and minimization in these frameworks rely on iteratively converging to a solution. Within each iteration the value of α changes based on the SALSA alternating direction maximization-minimization (ADMM) parameter, making it difficult to establish a relationship between α and data noise level with fractional- ℓ_1 /fraction-TV cases, however as explained in Algorithm-1 the fractional power was chosen automati-

cally with fractional- ℓ_1 /fraction-TV algorithms. Note that the ADMM reconstruction parameters were chosen empirically to result in best SNR/CNR, with standard ℓ_1 -norm, TV based reconstruction and in the proposed fractional ℓ_1 -norm/TV based reconstruction.

The fractional framework developed for ℓ_2 -norm, ℓ_1 -norm and TV minimization was superior to the state-of-the-art reconstruction methods. For high noise cases, the traditional model based algorithms seems to over-smooth the solution by decreasing the norm of the solution. The problem of over-smoothing can be mitigated by automatically choosing the fractional power in the developed fractional framework. The results presented in this work were unbiased as all reconstruction parameters in standard and proposed scheme were chosen to result in highest figure of merit value, i.e., SNR/CNR. Having the SVD matrix precomputed, the fractional Tikhonov, ℓ_1 -norm and TV based methods take about 101, 249, and 150 seconds to converge to the solution (including automatic fractional factor estimation) as opposed to 7.33, 184.89, and 185.25 seconds for standard Tikhonov, ℓ_1 -norm and TV schemes. Also, as it requires computation of the SVD of the model matrix, any change in the detection geometry requires recomputation of SVD, which is an computationally expensive procedure therefore implementing the same on graphics processing units will enable real-time **PAT**. It can be seen that automated choice of the fractional power requires about 100 seconds, while performing the reconstruction using Tikhonov method takes about 7 seconds, the process of automatically choosing the fractional power with simplex method can be parallelized using GPUs [56].

Recent emphasis in **PAT** is to develop handheld systems in two-[57], [58] and three-dimensions (3D) [33], these systems acquire data from one side of the sample and therefore will have limited coverage of the sample. Moreover these systems are found to add greater value in clinical and pre-clinical scenarios [59], [60]. The presented work has demonstrated the potential of fractional methods using a single element transducer with full 360 degree coverage (limited sensor positions) spanning the entire sample being imaged. The problem becomes more complex with handheld systems due to very less independent measurements in comparison to the experimental setting used in our study, therefore future work will involve studying the utility of the developed fractional framework with handheld configuration. Further, it is well known that using ℓ_1 -norm based framework could potentially accelerate **PA** image acquisition (along with data sampling methods) [32] enabling 3D imaging with frame-rates reaching few kilohertz. Hence performing data sampling studies in the context of fractional algorithms will add tremendous potential in realizing real-time 3D **PAT** imaging.

V. CONCLUSION

Model-based reconstruction algorithms improve the quantitative accuracy of **PA** images. This work introduced fractional regularization framework implemented for Tikhonov, ℓ_1 -norm and TV based algorithms to improve the reconstructed image quality in **PAT**. The fractional method is identical to standard Tikhonov, ℓ_1 -norm and TV regularization schemes when fractional parameter is taken as one making it more generic and appealing. The performance of the proposed fractional methods has been superior compared to standard state-of-the-art methods like Tikhonov, ℓ_1 -norm, and TV based reconstruction. The superior performance can be attributed to the inclusion of fractional power which controls the level of smoothness by increasing the norm of the reconstructed solution. Further the fractional power was chosen automatically using a simplex method by maximizing the SNR/CNR of the reconstructed **PA** image. The results indicate that the fractional power was inversely proportional to

the data noise level in the case of fractional Tikhonov scheme, same was proven both theoretically and found in numerical simulations. It was found that the fractional framework is superior to standard reconstruction methods (with improvement being as high as 54%) in numerical simulations, experimental phantom and *in vivo* rat data.

APPENDIX I CONTROLLING THE SMOOTHNESS WITH FRACTIONAL PARAMETER α

The singular vectors associated with small singular values usually contain high frequency oscillations. Analyzing the filter factors of fractional Tikhonov method (given in Eq. 21) for smaller singular values i.e., $\sigma \ll 1$ and expanding Eq. 21 using Taylor series and neglecting higher order term leads to,

$$\phi(\sigma) = \frac{\sigma^\alpha}{\lambda} - \frac{\sigma^{2\alpha+1}}{\lambda^2} \quad (32)$$

Considering $\phi_t(\alpha) = \sigma^\alpha$ in Eq. 32 as a function of α and differentiating with respect to α results in,

$$\phi'_t(\alpha) = \sigma^\alpha \ln(\sigma) \quad (33)$$

For this analysis, one can consider $\sigma \ll 1$ for which $\phi_t(\alpha)$ is a decreasing function as $\phi'_t(\alpha) < 0$ for $\sigma \ll 1$. Following this, each term in Eq. 32 is decreasing function of α . Thus, reducing the fraction power from $\alpha = 1$ (Tikhonov) increases $\phi(\sigma)$, implying increased high frequency contents in the fractional Tikhonov reconstructed solution (in other words, reducing the smoothness in the image).

APPENDIX II RELATIONSHIP OF α WITH NOISE

λ is a function of δ and can be derived from discrepancy principle given in Eq. 9. Substituting Eq. 20 in Eq. 9 and taking F as an $n \times m$ matrix with its diagonal elements being filter factors of fractional Tikhonov scheme, i.e., $\text{diag}(F) = \phi_{frac}(\sigma_i)$ results in,

$$\begin{aligned} \|\mathbf{U}\mathbf{U}^T \mathbf{b} - \mathbf{U}\mathbf{\Sigma}\mathbf{F}\mathbf{U}^T \mathbf{b}\|_2^2 &= \delta^2 \\ \|\mathbf{U}(\mathbf{I} - \mathbf{\Sigma}\mathbf{F})\mathbf{U}^T \mathbf{b}\|_2^2 &= \delta^2 \\ \left\| \sum_{i=1}^m (1 - \sigma_i \phi_{frac}(\sigma_i)) (u_i^T \mathbf{b}) u_i \right\|_2^2 &= \delta^2 \end{aligned} \quad (34)$$

Rewriting the above equation (considering $k = \min(m, n^2)$),

$$\begin{aligned} \sum_{i=1}^k (1 - \sigma_i \phi_{frac}(\sigma_i))^2 (u_i^T \mathbf{b})^2 + \sum_{j=k+1}^m (u_j^T \mathbf{b})^2 &= \delta^2 \\ \sum_{i=1}^k \frac{\lambda^2 \sigma_i^{\alpha+1}}{(\sigma_i^{\alpha+1} + \lambda)^2} (u_i^T \mathbf{b})^2 + \sum_{j=k+1}^m (u_j^T \mathbf{b})^2 &= \delta^2 \end{aligned} \quad (35)$$

Differentiating Eq. 35 w.r.t. λ , i.e. taking $\delta(\lambda)$ as an inverse function of $\lambda(\delta)$ results in,

$$2\delta(\lambda)\delta'(\lambda) = \sum_{i=1}^k \frac{2\lambda\sigma_i^{2\alpha+2}}{(\sigma_i^{\alpha+1} + \lambda)^3} (u_i^T \mathbf{b})^2 \quad (36)$$

It follows that $\delta'(\lambda) > 0$, i.e., $\delta(\lambda)$ is a monotonically increasing function, which implies the existence of its inverse $\lambda(\delta)$ being monotonically decreasing.

Hence the regularization parameter decreases with increasing noise. Now taking two different noise cases $\delta_1 > \delta_2$, one has $\lambda_1 < \lambda_2$. Considering two different filter factors corresponding to

each of the regularization parameters λ_1 and λ_2 in the fractional Tikhonov case results in,

$$\phi_1(\sigma) = \frac{\sigma^{\alpha_1}}{\lambda_1} - \frac{\sigma^{2\alpha_1+1}}{\lambda_1^2} \quad \phi_2(\sigma) = \frac{\sigma^{\alpha_2}}{\lambda_2} - \frac{\sigma^{2\alpha_2+1}}{\lambda_2^2} \quad (37)$$

Note that these filter factors are associated with lower singular values for the noise levels δ_1 and δ_2 correspondingly. From Eq. 37, one can establish that the filter factors are decreasing functions of λ . For the case of $\lambda_1 < \lambda_2$, the corresponding filter factors will be related as $\phi_1 > \phi_2$. This means that the high frequency contents are suppressed while performing reconstructions with noisy data (as $\lambda_1 < \lambda_2$ implies $\delta_1 > \delta_2$). Ideally one wants a solution with equal high frequency content both at high noise and low noise scenarios, implying $\phi_1 \approx \phi_2$. From Appendix-I, it is clear that increasing ϕ will reduce α , making $\alpha_1 < \alpha_2$. Therefore when $\delta_1 > \delta_2$, results in $\alpha_1 < \alpha_2$ i.e. fractional power reduces by increasing noise in the data.

APPENDIX III DIFFERENCE BETWEEN WEIGHTED- AND FRACTIONAL REGULARIZATION METHODS

Generalized Weighted Regularization:

In case of weighted Tikhonov scheme, the data fidelity term and regularization term in Eq. (4) can be penalized using weight matrices, which is given as,

$$\Gamma_{WTikh} = \min_x \left[((\mathbf{A}x - \mathbf{b})^T \mathbf{W}_b (\mathbf{A}x - \mathbf{b})) + \lambda (\mathbf{x}^T \mathbf{W}_x \mathbf{x}) \right] \quad (38)$$

where \mathbf{W}_b and \mathbf{W}_x are diagonal weight matrices corresponding to the data-fidelity and prior constraint, which are given as,

$$\mathbf{W}_b = (\text{COV}(\mathbf{A}\mathbf{x} - \mathbf{b}))^{-1}; \mathbf{W}_x = (\text{COV}(x))^{-1} \quad (39)$$

where COV indicates the covariance matrix. Differentiating Eq. (38) with respect to x and equating to zero results in,

$$((\mathbf{A}^T \mathbf{W}_b \mathbf{A}) + \lambda \mathbf{W}_x) x_{\text{general}} = (\mathbf{A}^T \mathbf{W}_b \mathbf{b}) \quad (40)$$

Using the SVD of \mathbf{A} in Eq. (40) results in,

$$(\mathbf{V}\mathbf{S}^T \mathbf{U}^T \mathbf{W}_b \mathbf{U}\mathbf{S}\mathbf{V}^T + \lambda \mathbf{W}_x) \mathbf{x}_{\text{general}} = \mathbf{V}\mathbf{S}^T \mathbf{U}^T \mathbf{W}_b \mathbf{b} \quad (41)$$

Assuming that we are weighting only the prior constraint i.e. $\mathbf{W}_b = \mathbf{I}$, we will get,

$$(\mathbf{V}\mathbf{S}^T \mathbf{U}^T \mathbf{U}\mathbf{S}\mathbf{V}^T + \lambda \mathbf{W}_x) \mathbf{x}_{\text{wx}} = \mathbf{V}\mathbf{S}^T \mathbf{U}^T \mathbf{b} \quad (42)$$

In other words, weighting the regularization term will lead to,

$$x_{wx} = (\mathbf{V}\mathbf{S}^T \mathbf{S}\mathbf{V}^T + \lambda \mathbf{W}_x)^{-1} \mathbf{V}\mathbf{S}^T \mathbf{U}^T \mathbf{b} \quad (43)$$

We can rewrite the above equation as,

$$x_{wx} = (\mathbf{V}\mathbf{S}^T \mathbf{S}\mathbf{V}^T + \lambda \mathbf{V}\mathbf{V}^T \mathbf{W}_x \mathbf{V}\mathbf{V}^T)^{-1} \mathbf{V}\mathbf{S}\mathbf{U}^T \mathbf{b} \quad (44)$$

Further, rearranging the terms results in,

$$x_{wx} = \mathbf{V}(\mathbf{S}^T \mathbf{S} + \lambda \mathbf{V}^T \mathbf{W}_x \mathbf{V})^{-1} \mathbf{S}\mathbf{U}^T \mathbf{b} \quad (45)$$

The solution is given by,

$$\begin{aligned} x_{wx} &= \sum_{i=1}^k \frac{\sigma_i}{\sigma_i^2 + \lambda v_i^T \mathbf{W}_x v_i} (u_i^T \mathbf{b}) v_i \\ &= \sum_{i=1}^k \phi_{wx}(\sigma_i) (u_i^T \mathbf{b}) v_i \end{aligned} \quad (46)$$

The filter function while weighting the regularization will be,

$$\phi_{wx}(\sigma) = \frac{\sigma_i}{\sigma_i^2 + \lambda v_i^T \mathbf{W}_x v_i} \quad (47)$$

On similar lines, we can write x_{wb} i.e. assuming $\mathbf{W}_x = \mathbf{I}$ as,

$$x_{wb} = \mathbf{V}(\mathbf{S}^T \mathbf{U}^T \mathbf{W}_b \mathbf{U} \mathbf{S} + \lambda \mathbf{I})^{-1} \mathbf{S}^T \mathbf{U}^T \mathbf{W}_b \mathbf{b} \quad (48)$$

The filter function while weighting the data-fidelity can be written as,

$$\phi_{wb}(\sigma) = \frac{\sigma_i w_b}{\sigma_i u_i^T w_b u_i \sigma_i + \lambda} \quad (49)$$

Fractional Regularization Method:

In case of fractional Tikhonov scheme, the data fidelity term in Eq. (4) is penalized using fractional power and can be rewritten as,

$$\Gamma_{frac} = \min_x (\|\mathbf{A}x - \mathbf{b}\|_{\mathbf{W}}^2 + \lambda \|x\|_2^2) \quad (50)$$

where, $\|x\|_{\mathbf{W}} = (x^T \mathbf{W} x)^{\frac{1}{2}}$ and \mathbf{W} is symmetric positive semidefinite matrix given as,

$$\mathbf{W} = (\mathbf{A} \mathbf{A}^T)^{\frac{(\alpha-1)}{2}} \quad (51)$$

where, α represents the fractional power with $\alpha > 0$. Differentiating Eq. (50) with respect to x and equating to zero results in,

$$((\mathbf{A}^T \mathbf{A})^{(\alpha+1)/2} + \lambda \mathbf{I}) x = (\mathbf{A}^T \mathbf{A})^{(\alpha-1)/2} \mathbf{A}^T \mathbf{b} \quad (52)$$

The final solution is given by,

$$\begin{aligned} x_{frac} &= \sum_{i=1}^k \frac{\sigma_i^\alpha}{\sigma_i^{\alpha+1} + \lambda} (u_i^T \mathbf{b}) v_i \\ &= \sum_{i=1}^k \phi_{frac}(\sigma_i) (u_i^T \mathbf{b}) v_i \end{aligned} \quad (53)$$

The filter function of fractional Tikhonov method for $\alpha > 0$ is given by,

$$\phi_{frac}(\sigma) = \frac{\sigma^\alpha}{\sigma^{\alpha+1} + \lambda} \quad (54)$$

Comparing Eq. (46), Eq. (49) and Eq. (54), it is clear that the weighted regularization indeed scales or shifts the singular values based on the weight matrix entries, in contrary the fractional method raises the singular value to fractional power.

REFERENCES

- [1] L. H. V. Wang, and S. Hu, "Photoacoustic tomography: In Vivo Imaging from Organelles to Organs," *Science*, vol. 335, pp. 1458-1462, Mar. 2012.
- [2] A. A. Karabutov, E. V. Savateeva, and A. A. Oraevsk, "Optoacoustic tomography: new modality of laser diagnostic systems," *Laser Phys.*, vol. 13, pp. 711723, May 2003.
- [3] P. K. Upputuri, and M. Pramanik, "Recent advances towards preclinical and clinical translation of photoacoustic tomography: a review," *J. Biomed. Opt.*, vol. 22, no. 4, 041006 Nov. 2017.
- [4] L. Li et al., "Single-impulse panoramic photoacoustic computed tomography of small-animal whole-body dynamics at high spatiotemporal resolution," *Nat. Biomed. Engg.*, vol. 1, no. 5, May 2017.
- [5] L. V. Wang, and J. Yao, "A practical guide to photoacoustic tomography in the life sciences," *Nat. Meth.*, vol. 13, no. 8, pp. 627-638, Jul. 2016.
- [6] V. Ntziachristos, "Going deeper than microscopy: the optical imaging frontier in biology," *Nat. Meth.*, vol. 7, no. 8, p. 603, Aug. 2010.
- [7] P. K. Upputuri, and M. Pramanik, "Dynamic in vivo imaging of small animal brain using pulsed laser diode-based photoacoustic tomography system," *J. Biomed. Opt.*, vol. 22, no. 9, p. 090501, Sep. 2017.
- [8] H. F. Zhang, K. Maslov, G. Stoica, and L. H. V. Wang, "Functional photoacoustic microscopy for high-resolution and noninvasive in vivo imaging," *Nat. Biotech.*, vol. 24, pp. 848-851, Jul. 2006.
- [9] B. Yin, D. Xing, Y. Wang, Y. Zeng, Y. Tan, and Q. Chen, "Fast photoacoustic imaging system based on 320-element linear transducer array," *Phys. Med. Bio.*, vol. 49, pp. 1339-1346, Apr. 2004.
- [10] M. Pramanik, and L. H. V. Wang, "Thermoacoustic and photoacoustic sensing of temperature," *J. Biomed. Opt.*, vol. 14, p. 054024, Oct. 2009.
- [11] K. H. Song, and L. H. V. Wang, "Noninvasive photoacoustic imaging of the thoracic cavity and the kidney in small and large animals," *Med. Phys.*, vol. 35, pp. 4524-4529, Oct. 2008.
- [12] D. Yang, D. Xing, S. Yang and L. Xiang, "Fast full-view photoacoustic imaging by combined scanning with a linear transducer array," *Opt. Express*, vol. 15, p. 15566, 2007.
- [13] S. Yang, D. Xing, Q. Zhou, L. Xiang, and Y. Lao, "Functional imaging of cerebrovascular activities in small animals using high-resolution photoacoustic tomography," *Med. Phys.*, vol. 34, pp. 3294-3301, 2007.
- [14] S. Yang, D. Xing, Y. Lao, D. Yang, L. Zeng, L. Xiang and W. R. Chen, "Noninvasive monitoring of traumatic brain injury and post-traumatic rehabilitation with laser-induced photoacoustic imaging," *Appl. Phys. Lett.*, vol. 90, p. 243902, 2007.
- [15] Y. Zhou, J. Yao, and L. V. Wang, "Tutorial on photoacoustic tomography," *J. Biomed. Opt.*, vol. 21, p. 061007, Jun. 2016.
- [16] C. Kim, C. Favazza, and L. V. Wang, "In vivo photoacoustic tomography of chemicals: high-resolution functional and molecular optical imaging at new depths," *Chem. Rev.*, vol. 110, pp. 2756-2782, May 2010.
- [17] V. Gujrati, A. Mishra, and V. Ntziachristos, "Molecular imaging probes for multi-spectral optoacoustic tomography," *Chem. Comm.*, vol. 53, no. 34, pp. 4653-4672, Mar. 2017.
- [18] J. Prakash, A. S. Raju, C. B. Shaw, M. Pramanik, and P. K. Yalavarthy, "Basis pursuit deconvolution for improving model-based reconstructed images in photoacoustic tomography," *Biomed. Opt. Exp.*, vol. 5, pp. 1363-1377, May 2014.
- [19] M. Bhatt, S. Gutta, and P. K. Yalavarthy, "Exponential filtering of singular values improves photoacoustic image reconstruction," *J. Opt. Soc. Am. A* vol. 33, pp. 1785-1792, Sep. 2016.
- [20] A. Rosenthal, V. Ntziachristos, and D. Razansky, "Acoustic inversion in optoacoustic tomography: a review," *Curr. Med. Imag. Rev.* vol. 9, pp. 318-336, Nov. 2013.
- [21] R. Aster, B. Borchers, and C. Thurber, *Parameter Estimation and Inverse Problem*, vol. 90, Elsevier Academic Press, 2005.
- [22] K. Wang, S. A. Ermilov, R. Su, H. P. Brecht, A. A. Oraevsky, and M. A. Anastasio, "An imaging model incorporating ultrasonic transducer properties for three-dimensional optoacoustic tomography," *IEEE Trans. Med. Imag.*, vol. 30, no. 2, pp. 203-214, Feb. 2011.
- [23] A. Buehler, A. Rosenthal, T. Jetzfellner, A. Dima, D. Razansky, and V. Ntziachristos, "Model-based optoacoustic inversions with incomplete projection data," *Med. Phys.*, vol. 38, pp. 1694-1704, Mar. 2011.
- [24] K. Wang, R. Su, A. A. Oraevsky, and M. A. Anastasio, "Investigation of iterative image reconstruction in three dimensional optoacoustic tomography," *Phys. Med. Biol.*, vol. 57, pp. 5399-5423, Aug. 2012.
- [25] P. C. Hansen, *Rank-deficient and discrete ill-posed problems: numerical aspects of linear inversion*, SIAM, 1998.
- [26] X. L. Dean-Ben, A. Buehler, V. Ntziachristos, and D. Razansky, "Accurate model-based reconstruction algorithm for three-dimensional optoacoustic tomography," *IEEE Trans. Med. Imag.*, vol. 31, no. 10, pp. 1922-1928, Oct. 2012.
- [27] G. Paltauf, J. A. Viator, S. A. Prahl, and S. L. Jacques, "Iterative reconstruction algorithm for optoacoustic imaging," *J. Acous. Soc. Am.*, vol. 112, pp. 1536-1544, Oct. 2002.
- [28] C. B. Shaw, J. Prakash, M. Pramanik, and P. K. Yalavarthy, "Least squares QR-based decomposition provides an efficient way of computing optimal regularization parameter in photoacoustic tomography," *J. Biomed. Opt.*, vol. 18, p. 080501, May 2013.
- [29] S. Tzoumas, A. Rosenthal, C. Lutzweiler, D. Razansky, and V. Ntziachristos, "Spatiospectral denoising framework for multispectral optoacoustic imaging based on sparse signal representation," *Med. Phys.* vol. 41 2014.
- [30] I. Olefir, S. Tzoumas, H. Yang and V. Ntziachristos, "Bayesian Approach to Eigenspectra Optoacoustic Tomography," *IEEE Trans. Med. Imag.* vol. 37, pp. 2070-2079, 2018.
- [31] V. A. Morozov, *Methods for Solving Incorrectly Posed Problems*, Springer New York, 1984.
- [32] A. Ozbek, X. L. Den-Ben, and D. Razansky, "Optoacoustic imaging at kilohertz volumetric frame rates," *Optica*, vol. 5, pp. 857-863, Jul. 2018.
- [33] Y. Han, L. Ding, X. L. D. Ben, D. Razansky, J. Prakash, and V. Ntziachristos, "Three-dimensional optoacoustic reconstruction using fast sparse representation," *Opt. Lett.*, vol. 42, pp. 979-982, Feb. 2017.
- [34] N. Awasthi, S. K. Kalva, M. Pramanik, and P. K. Yalavarthy, "Vector Extrapolation Methods for Accelerating Iterative Reconstruction Methods in Limited-Data Photoacoustic Tomography," *J. Biomed. Opt.* vol. 23, no. 7, p. 071204, Feb. 2018.
- [35] J. Provost, and F. Lesage, "The application of compressed sensing for photo-acoustic tomography," *IEEE Trans. Med. Imag.*, vol. 28, no. 4, pp. 585-594, Apr. 2009.
- [36] M. E. Hochstenbach, and L. Reichel, "Fractional Tikhonov regularization for linear discrete ill-posed problems," *BIT Numer. Math.*, vol. 51, no. 1, pp. 197-215, Mar. 2011.

- [37] E. Klann, and R. Ramlau, "Regularization by fractional filter methods and data smoothing," *Inv. Problems*, vol. 24, p. 025018, Feb. 2008.
- [38] L. V. Wang and H.-I. Wu, "Photoacoustic tomography," *Biomedical optics: principles and imaging*, John Wiley & Sons, 2012.
- [39] B. E. Treeby, and B. T. Cox, "k-Wave: MATLAB toolbox for the simulation and reconstruction of photoacoustic wavefields," *J. Biomed. Opt.*, vol. 15, p. 021314, Mar. 2010.
- [40] N. Awasthi, S. K. Kalva, M. Pramanik, and Phaneendra K Yalavarthy, "Image Guided Filtering for Improving Photoacoustic Tomographic Image Reconstruction," *J. Biomed. Opt.*, vol. 23 no. 9, p. 091413, Sep. 2018.
- [41] G. L. Zeng, "Medical Image Reconstruction: A Conceptual Tutorial," Springer, New York (2010).
- [42] R. P. K. Jagannath and P. K. Yalavarthy, "Minimal residual method provides optimal regularization parameter for diffuse optical tomography," *J. Biomed. Opt.*, vol. 17, p. 106015, Mar. 2012.
- [43] P. C. Hansen, "Regularization tools version 4.0 for Matlab 7.3," *Numer. Algo.*, vol. 46, no. 2, pp. 189-194, Oct. 2007.
- [44] J. Prakash, C. B. Shaw, R. Manjappa, R. Kanhirodan, and P. K. Yalavarthy, "Sparse Recovery Methods Hold Promise for Diffuse Optical Tomographic Image Reconstruction," *IEEE J. Sel. Top. Quant. Elec.*, vol. 24, no. 2, p. 6800609, Feb. 2014.
- [45] H. He, J. Prakash, A. Buehler, and V. Ntziachristos, "Optoacoustic Tomography Using Accelerated Sparse Recovery and Coherence Factor Weighting," *Tomography*, vol. 2 no.2, pp. 138-145, June 2016.
- [46] M. V. Afonso, J. M. Bioucas-Dias, and M. A. T. Figueiredo, "Fast image recovery using variable splitting and constrained optimization," *IEEE Trans. Image Process.*, vol. 19 no. 9, pp. 2345-2356, Sep. 2010.
- [47] Y. Han, S. Tzoumas, A. Nunes, V. Ntziachristos, and A. Rosenthal, "Sparsitybased acoustic inversion in crosssectional multiscale optoacoustic imaging," *Med. Phys.*, vol. 42 no. 9, pp. 5444-5452, Sep. 2015.
- [48] K. Wang, E. Y. Sidky, M. A. Anastasio, A. A. Oraevsky, and X. Pan, "Limited data image reconstruction in optoacoustic tomography by constrained total variation minimization," *SPIE Photons Plus Ultrasound: Imaging and Sensing*, vol. 7899, pp. 78993, Feb. 2011.
- [49] L. Yao, and H. Jiang, "Enhancing finite element-based photoacoustic tomography using total variation minimization," *App. Opt.*, vol. 50 no. 25, pp. 5031-5041, Sep. 2011.
- [50] A. Chambolle, "An algorithm for total variation minimization and applications," *J. Math. Imag. Vision*, vol. 20 no. 1, pp. 89-97, Jan. 2004.
- [51] X. Song, B. W. Pogue, S. Jiang, M. M. Doyley, H. Dehghani, T. D. Tosteson, and K. D. Paulsen, "Automated region detection based on the contrast-to-noise ration in near-infrared tomography," *App. Opt.*, vol. 43 no. 5, pp. 1053-1062, Feb. 2004.
- [52] Y. Lou, W. Zhou, T. P. Matthews, C. M. Appleton, and M. A. Anastasio, "Generation of anatomically realistic numerical phantoms for photoacoustic and ultrasonic breast imaging," *J. Biomed. Opt.*, vol. 22 no. 4, p. 041015, Apr. 2017.
- [53] American National Standard for Safe Use of Lasers ANSI Z136.1-2000.
- [54] P. K. Upputuri and M. Pramanik, "Pulsed laser diode based optoacoustic imaging of biological tissues," *Biomed. Phys. Eng. Exp.*, vol. 1 no. 4, p. 045010 Dec. 2015.
- [55] P. K. Yalavarthy, B. W. Pogue, H. Dehghani, and K. D. Paulsen, "Weight-Matrix Structured Regularization Provides Optimal Generalized Least Squares Estimate in Diffuse Optical Tomography," *Med. Phys.* vol. 34 no. 6, pp. 2085-2098 June 2007.
- [56] N. Ploskas and N. Samaras, "Efficient GPU-based implementations of simplex type algorithms," *App. Math. Comp.*, vol. 250, pp. 552-570 2015.
- [57] V. Neuschmelting, et. al., "WST11 Vascular Targeted Photodynamic Therapy Effect Monitoring by Multispectral Optoacoustic Tomography (MSOT) in Mice," *Thno*, vol. 8 no. 3, pp. 723-734, Mar. 2018.
- [58] P. Hajireza, A. Forbrich, and R. Zemp, "In-Vivo functional optical-resolution photoacoustic microscopy with stimulated Raman scattering fiber-laser source," *Biomed. Opt. Exp.*, vol. 5 no. 2, pp. 539-546, Feb. 2014.
- [59] G. Diot et. al., "Multi-Spectral Optoacoustic Tomography (MSOT) of human breast cancer," *Clinical Cancer Research*, vol. 23 no. 22, pp. 6912-6922, Nov. 2017.
- [60] F. Knieling et. al., "Multispectral optoacoustic tomography for assessment of Crohns disease activity," *N. Engl. J. Med.*, vol. 376 no. 13, pp. 1292-1294, Mar. 2017.